An updated seabed bathymetry beneath Larsen C Ice Shelf, west Antarctica

Alex Brisbourne[1], Bernd Kulessa[2], Thomas Hudson[1], Lianne Harrison[1], Paul Holland[1], Adrian Luckman[2], Suzanne Bevan[2], David Ashmore[3], Bryn Hubbard[4], Emma Pearce[5], James White[6], Adam Booth[5], Keith Nicholls[1] and Andrew Smith[1]

[1]British Antarctic Survey, Natural Environment Research Council, Madingley Road, Cambridge, CB3 0ET, UK.
[2]Glaciology Group, College of Science, Swansea University, Singleton Park, Swansea SA2 8PP, UK
[3]School of Environmental Sciences, University of Liverpool, Liverpool, L69 7ZT, UK
[4]Centre for Glaciology, Department of Geography and Earth Sciences, Aberystwyth University, Aberystwyth, SY23 3DB, UK
[5]Department of Earth and Environment, University of Leeds, Leeds, LS2 9JT, UK
[6]British Geological Survey, Keyworth, Nottingham, NG12 5GG, UK

Correspondence to: Alex Brisbourne (aleisb@bas.ac.uk)

Abstract. In recent decades, rapid ice-shelf disintegration along the Antarctic Peninsula has had a global impact through enhancing outlet glacier flow, and hence sea level rise, and the freshening of Antarctic Bottom Water. Ice shelf thinning due to basal melting results from the circulation of relatively warm water in the underlying ocean cavity. However, the effect of sub-shelf circulation on future ice-shelf stability cannot be predicted accurately with computer simulations if the geometry of the ice-shelf cavity is unknown. To address this deficit for Larsen C Ice Shelf, west Antarctica, we integrate new water-column thickness measurements with existing observations. We present these new data here along with an updated bathymetry grid of the ocean cavity. Key findings include relatively deep seabed to the south-east of the Kenyon Peninsula, along the grounding line and around the key ice shelf pinning point of Bawden Ice Rise. In addition, we can confirm that the cavity's southern trough stretches from Mobiloil Inlet to the open ocean. These areas of deep seabed will influence ocean circulation and tidal mixing, and will therefore affect the basal-melt distribution. These results will help constrain models of ice-shelf cavity circulation with the aim of improving our understanding of sub-shelf processes and their potential influence on ice shelf stability. The data set comprises all point measurements of seabed depth and a gridded data product, derived using additional measurements of both offshore seabed depth and the thickness of grounded ice. We present all new depth measurements here as well as a compilation of previously published measurements used in the gridding process. The gridded data product is included in the supplementary material.

The underlying seismic data sets which were used to determine bed depth and ice thickness are available at
https://doi.org/10.5285/315740B1-A7B9-4CF0-9521-86F046E33E9A (Brisbourne et al., 2019),
https://doi.org/10.5285/5D63777D-B375-4791-918F-9A5527093298 (Booth, 2019), https://doi.org/10.5285/FFF8AFEE-4978-495E-9210-120872983A8D
(Kulessa and Bevan, 2019) and https://doi.org/10.5285/147BAF64-B9AF-4A97-8091-26AEC0D3C0BB (Booth et al., 2019).

1 Introduction

The loss of Antarctic ice shelves is of global significance for two reasons. First, ice shelves provide a buttressing force – controlled by the geometry and stress regime of the ice shelf - to the glaciers or ice streams that feed them. Although loss of the floating ice shelf makes only a small direct contribution to sea level rise, the removal of buttressing results in acceleration

5 of the tributary glaciers, enhancing their current contribution to sea level rise (Rignot et al., 2004; Scambos et al., 2004). Secondly, basal melting of ice shelves produces cold and low-salinity water that influences Antarctic Bottom Water (AABW) formation, which in turn affects the properties of the global oceans (Jacobs, 2004).

Over recent decades, there has been a southwards progression of ice shelf loss along the eastern Antarctic Peninsula. The
10 disintegration of the Larsen A Ice Shelf in 1995, and the Larsen B in 2002, resulted in a step increase in flow of the grounded glaciers that formerly fed these ice shelves (e.g., Khazendar et al., 2015). This increase in glacier flow resulted in accelerated sea level rise and increased freshening of dense AABW (Jullion et al., 2013). In a number of cases, ice shelf retreat has been attributed to atmospheric warming (Vaughan and Doake, 1996; Rott et al., 1998; Skvarca et al., 1999). With the Antarctic Peninsula exhibiting one of Earth's highest rates of atmospheric warming during the late twentieth century, the long-term
15 viability of the Larsen C Ice Shelf (LCIS) is in question. However, Holland et al. (2015) demonstrated that the thinning of LCIS over the last decade is a result of both atmospheric and oceanic influence in almost equal measure. For the remaining ice shelves on the Antarctic Peninsula, the relative contribution to their future stability by basal melt from incursions of relatively warm ocean water, and increased surface melting by a warmer atmosphere, is still unknown.

20 To improve projections of the effects of basal melt on ice shelves, knowledge of the geometry of the ocean cavity beneath is vital (Mueller et al., 2012; Jenkins et al., 2010; Grosfeld et al., 1997). Models of sub-shelf circulation are critically dependent on cavity geometry, particularly in regions where the influence of strong tides is topographically constrained (e.g., Mueller et al., 2012). Ongoing efforts to model ocean processes beneath LCIS suffer from inadequate knowledge of cavity geometry because seabed depth is very poorly sampled (Brisbourne et al., 2014). Improving knowledge of cavity geometry is crucial for
25 LCIS because the sparse existing data suggest the presence of large-scale seabed features capable of guiding ocean currents and inducing significant tidal mixing. It is impossible for computer simulations to predict accurately the future influence of the ocean on LCIS without knowledge of the geometry of such features.

2 Location and previous work

LCIS, the largest ice shelf on the Antarctic Peninsula at around 44 000 km^2 (Cook and Vaughan, 2010), lies just south of the
30 recently collapsed Larsen A and B ice shelves (Fig. 1). The geometry of LCIS's sub-shelf cavity has previously been measured in detail at specific locations only (Brisbourne et al., 2014) where an inversion of gravity measurements indicated areas of significant control over sub-shelf circulation (Cochran and Bell, 2012). However, uncertainties associated with such inversions

for bathymetry result in large areas of unknown geometry, specifically beneath LCIS (i) away from the western grounding line, (ii) away from the ice front, and (iii) in the south.

We build on a number of published sources of bathymetry data with new observations from four recent field campaigns. The existing bathymetry data used in the gridding process here are derived from a targeted seismic bathymetry survey, seismic refraction experiments and drill site measurements (Brisbourne et al., 2014). The depth to grounded ice and known offshore bathymetry of Bedmap2 is included in the gridding process (Fretwell et al., 2013). Surface elevation and ice thickness measurements at Bawden Ice Rise are also included (Holland et al., 2015). Here, we integrate these existing data with the new measurements of seabed depth. All data are then gridded to obtain a new bathymetry map of LCIS.

3 Data acquisition and processing

3.1 Data Acquisition

In December 2016, 14 seismic bathymetry measurements were made across LCIS, targeting areas of sparse data coverage. The seismic source consisted of a sledgehammer with a plate stamped into the snow surface, or dug down to a shallow ice layer, to improve source consistency. Twenty-four Georod receivers (Voigt et al., 2013) were buried to 30 cm depth at 10 m spacing with a 30 m offset to the first receiver. Burying sensors in this way ensures good coupling and provides protection from wind-induced noise. Georods consist of four geophone elements in series, which improves the signal to noise ratio. We recorded 2 s records at 0.125 ms sample interval with a 24-channel data logger. At each site, ~20 hammer blows were recorded using a geophone trigger adjacent to the hammer plate. A stack of 10 hammer blows was also recorded for on-site evaluation of the seismic reflection strength. To determine an accurate surface elevation a dual-frequency GPS system ran for the duration of the seismic acquisition at each site.

These data are supplemented by bathymetry measurements from an additional 16 seismic refraction and reflection surveys across LCIS. Although many of these experiments targeted depth profiles of the firn, the data are suitable for ice shelf thickness and seabed depth measurement. The acquisition procedure is similar to that described above and therefore data quality and uncertainties are similar. Details of the acquisition parameters for each experiment are presented in Table 1.

Figure 2 presents an example of a seismic gather formed of 10 hammer blows stacked during acquisition. Clear ice base and seabed arrivals, as well as multiples thereof, are observed. Where necessary, to help identify reflections, a frequency-wavenumber filter was used to suppress groundroll that may mask the ice base reflection. An automatic gain control filter and semblance analysis was also used as required to constrain arrivals. However, ice base and seabed reflection traveltimes were measured on raw seismic records, even if a filter was required to help identify arrivals. A relatively thin ice shelf will result in

the ice base reflection arriving within groundroll noise. In these cases, surface multiples of the ice base reflection were used to calculate the primary two-way traveltime through the ice column.

3.2 Seismic velocities in ice and water and thickness measurement

5   Values of seismic velocity are required to convert traveltimes to layer thickness or depth. A mean seismic velocity in the water column of 1445 ± 1 m s^{-1} was derived during conductivity-temperature-depth (CTD) measurements made beneath northern and southern LCIS by Nicholls et al. (2012).

The seismic velocity profile in the upper 100 m of the ice shelf, which includes the firn, was measured using the shallow
10   refraction experiments presented here, as well as those of Brisbourne et al. (2014). At each of the refraction sites, a series of surface shots was recorded with increasing receiver spacing. The first arrivals were picked and converted to a velocity-depth profile using the method described by Kirchner and Bentley (1990). This method relies on a monotonic increase in velocity with depth, an assumption that is supported by observations of smoothly varying traveltimes. Below 100 m depth, we assume that ice density is constant and seismic velocity depends on ice temperature alone. CTD measurements of Nicholls et al. (2012)
15   indicate an ice-base temperature of -2° C. Therefore, below 100 m we linearly interpolate between the velocity measured by seismic refraction at 100 m depth and an ice base velocity calculated from the temperature-velocity relationship of Kohnen (1974). Where a bathymetry measurement and seismic refraction experiment are not coincident, results from the closest seismic refraction experiment are used to determine ice thickness.

20   Measurement of the surface elevation allows for the estimation of ice thickness assuming freely floating ice. These estimates can guide the identification of ice base reflections in the data. The EIGEN-GL04C geoid level (Forste et al., 2008) is removed from the elevation and an empirical relationship determined by Brisbourne et al. (2014) used to calculate ice thickness: geoid-corrected height, $h = 0.113H + 5.003$, where H is ice column thickness in metres. This relationship accounts for firn thickness, which affects mean density. The absence of a clear ice base reflection is not necessarily a result of poor data quality. Under
25   certain conditions, particularly in ice shelf suture zones, poorly consolidated marine ice at the base of the ice shelf may result in a weak or absent seismic reflection. At site PRHB4, in the absence of a clear ice base reflection, we calculate the ice thickness from the surface elevation using the empirical relationship described above.

3.3 Uncertainties

30   Errors in picking reflections, seismic velocities and seabed topography all contribute to uncertainties in ice and water-column thickness calculations.

Picking errors in the seismic reflection data are < 1 ms, equivalent to thickness uncertainties of 1.4 and 3.8 m for water and ice, respectively.

A conservative estimate of the uncertainties in seismic velocity in the ice column of 30 m s^{-1} (Kirchner and Bentley, 1990;
5   Rosier et al., 2018) is equivalent to an uncertainty of 2 m in ice column thickness. However, the presence of marine ice in suture zones (Kulessa, 2019) or significant warm refrozen ice within the firn column (Hubbard et al., 2016; Ashmore et al., 2017) may result in seismic velocities which deviate from the standard model and introduce greater uncertainty in measured velocities. However, a previous study highlighted the consistency between seismic-derived ice thickness measurements and those from surface elevation measurements (Brisbourne et al., 2014). Importantly, the thickness of the derived water column
10   is independent of the ice velocity-depth profile used. Direct measurements of seismic velocity in the water column (Nicholls et al., 2012) result in a much lower uncertainty in water column thickness than that of ice thickness or seabed depth.

Ice base and seabed topography can introduce additional uncertainty to thickness measurements (Nost, 2004). Calculations of ice and water column thickness from traveltimes assumes that reflectors are planar and horizontal. Such a geometry results in
15   a characteristic curvature, or moveout, of traveltimes with increasing receiver offset. Assuming an isotropic seismic velocity structure, any deviation from standard moveout is indicative of dip at the reflecting interface. Brisbourne et al. (2014) used observed deviations from standard moveout to demonstrate that topography across LCIS causes a maximum error in seabed depth of <10 m.

20   We calculate seabed depth by removing ice and water cavity thickness from measured surface elevation data. Elevation uncertainties in dual-frequency GPS measurements are ±40 mm. Where direct surface elevation measurements are not available the REMA surface DEM of 2017 at 8 m resolution is used (Howat et al., 2019), resulting in an absolute elevation uncertainty in these areas of ± 2 m. No tidal correction is made to surface elevations, resulting in a further uncertainty in surface elevation of ± 2 m (Brisbourne et al., 2014).

25

We therefore assign a maximum overall uncertainty of ±10 m to the calculated seabed depths.

4 Bathymetry gridding

We interpolated all available seabed depth measurements, along with grounded-ice depths and offshore bathymetry, to create
30   a map of the seabed geometry directly under the ice shelf. We present a 1.3 km horizontal resolution bathymetry map of LCIS's cavity created using a composite of the data outlined above and previously published depth measurements (Table A1). We use a natural neighbour interpolation, which is well suited to a dataset with an uneven distribution of data points. Importantly, the fit to these points does not 'overshoot', which would result in interpolated values that are higher or lower than known values.

Locations where the calculated seabed depth is shallower than the better-constrained ice draft of the Bedmap2 dataset (Fretwell et al., 2013) highlight the limitations of the data and gridding process. This issue is most noticeable along the grounding line, where bed topography changes rapidly but data coverage remains sparse. Therefore, in the gridded product we deepen the seabed where required to ensure that its depth is greater than the Bedmap2 ice draft plus an arbitrary minimum water column thickness of 10 m. This ensures that all interpolated seabed depths are at least consistent with known ice thickness measurements, which are regarded as far more reliable.

5 Results and significance of the data set

Figure 3 presents a map of seabed elevation in the LCIS region, resulting from gridding of all available data as described above. A number of key features that will influence tidal and oceanic circulation through the sub-shelf cavity, and thus affect basal melt rates and melt water circulation are apparent: (1) A relatively deep seabed surrounds Bawden Ice Rise (BIR), a key pinning point of LCIS. Holland et al. (2015) highlighted that BIR is the pinning point where LCIS is closest to floatation. The bathymetry of this area therefore plays a key role in the ice shelf's future stability. A deep seabed here may alter the strong tidal currents that are thought to induce melt in this region (Mueller et al., 2012). (2) The southern trough, to the north of the Kenyon Peninsula, extends from Mobiloil Inlet to the ice front. Nicholls et al. (2012) highlighted this deepening in southern LCIS as a potential conduit for High Salinity Shelf Water (HSSW) that may access the deeper ice at the grounding line, providing vigorous melting. Similarly, the updated bathymetry also confirms that the Jason Trough in the north also continues through to the open ocean, to the north of Bawden Ice Rise. (3) The sub-shelf cavity to the southeast of the Kenyon Peninsula is relatively deep. Again, Nicholls et al. (2012) highlight this location as potentially important to the supply of HSSW that sustains melt at the grounding line. (4) All additional point measurements confirm that the sub-shelf cavity is particularly deep close to the grounding line between Mobiloil Inlet and the Cole Peninsula. Sub-shelf circulation models highlight that the grounding line, where shelf ice is thickest and therefore deepest, provides a key site for basal melt.

The interaction of these newly determined cavity features with the sub-shelf circulation pattern requires detailed oceanic modelling to ascertain their importance. These data, along with the gridded bathymetry map, provide a valuable product for the study of ice-ocean interaction beneath LCIS. The updated bathymetry is a prerequisite to estimating the contribution of sub-shelf melt to thinning of the ice shelf and the contribution of that melt to the global ocean system. Previous studies have highlighted the importance of accurate bathymetry beneath LCIS, but until now have lacked information on the major troughs delineated by our data. The provision of the spot measurements will allow users to re-grid using other algorithms if required, and allow for rapid assimilation of any new data points that become available in the future. This is of course not a definitive data set and additional data points that address gaps in the current coverage will always be of value to reduce uncertainty where interpolation has been necessary. As the resolution of ocean models improves, the requirement for greater certainty with regards small-scale features will also increase.

Data Availability

The underlying seismic data sets which were used to determine bed depth and ice thickness are available at
https://doi.org/10.5285/315740B1-A7B9-4CF0-9521-86F046E33E9A (Brisbourne et al., 2019),
https://doi.org/10.5285/5D63777D-B375-4791-918F-9A5527093298 (Booth, 2019),

5 https://doi.org/10.5285/FFF8AFEE-4978-495E-9210-120872983A8D
 (Kulessa and Bevan, 2019) and   https://doi.org/10.5285/147BAF64-B9AF-4A97-8091-26AEC0D3C0BB

(Booth et al., 2019).

Author contribution

PRH and AMB led the NERC BAS bathymetry experiment. BK, AJL and ADB respectively led NERC projects SOLIS,
10 MIDAS and RACE. TH, BK, SB, DA, BH, AJL, ADB, EP and JW were involved in field data acquisition. AMB and BK
wrote the manuscript with contributions from others. LH and AMB gridded the final bathymetry product.

Competing interests

The authors declare no competing interests.

15 **Acknowledgements**

We acknowledge support by UK Natural Environment Research Council (NERC), the British Antarctic Survey Polar Science
for Planet Earth Programme and NERC grants NE/E012914/1 (SOLIS), NE/L005409/1 (MIDAS) and NE/R012334/1 (RACE)
and. We thank BAS Operations for support of all data acquisition presented here. NERC Geophysical Equipment Facility
supplied instruments for the fieldwork under loans 863, 864, 865, 1028 and 1060. The MODIS image from 2018 was retrieved
20 on 2019_10_01 from Earth Science Data and Information System (ESDIS) Project, Earth Science Projects Division (ESPD),
Flight Projects Directorate, Goddard Space Flight Center (GSFC) National Aeronautics and Space Administration (NASA)
2019.

Figures
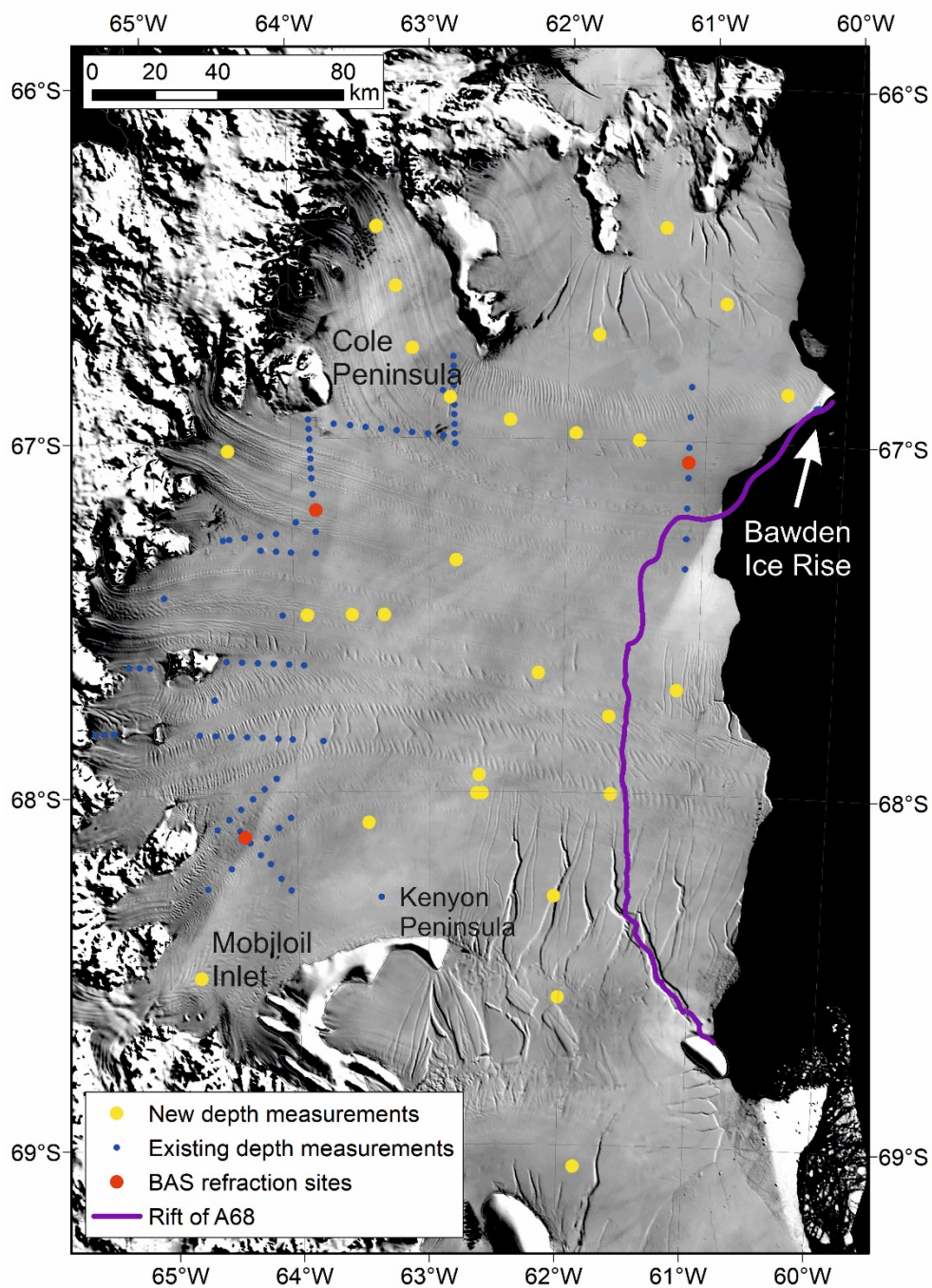
Figure 1 Map of seismic points used in the gridded bathymetry product of this study. The approximate path of the ice-shelf rift which resulted in the calving of iceberg A68 is highlighted (Jansen et al., 2015). The background is MODIS imagery
5   (Scambos et al., 2007), pre-dating the break-off of iceberg A68 along the rift.
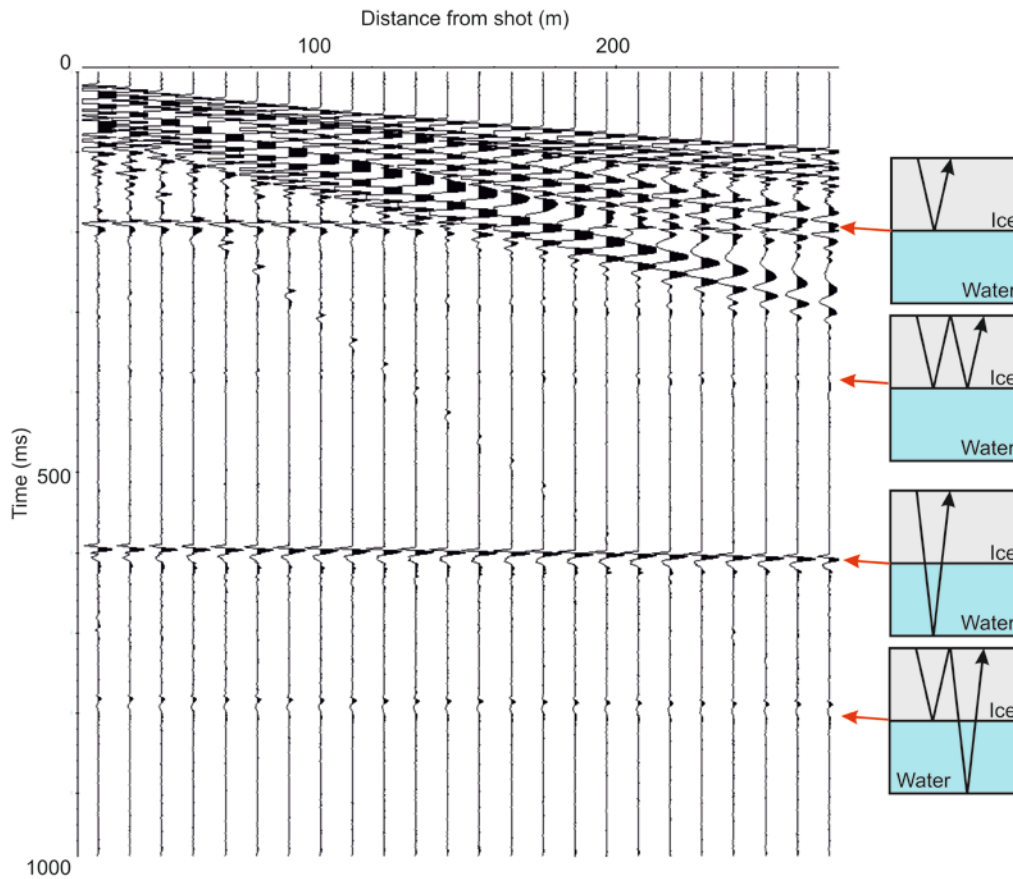
Figure 2 Example hammer and plate seismic shot gather with readily identified primary seismic reflections and multiples.
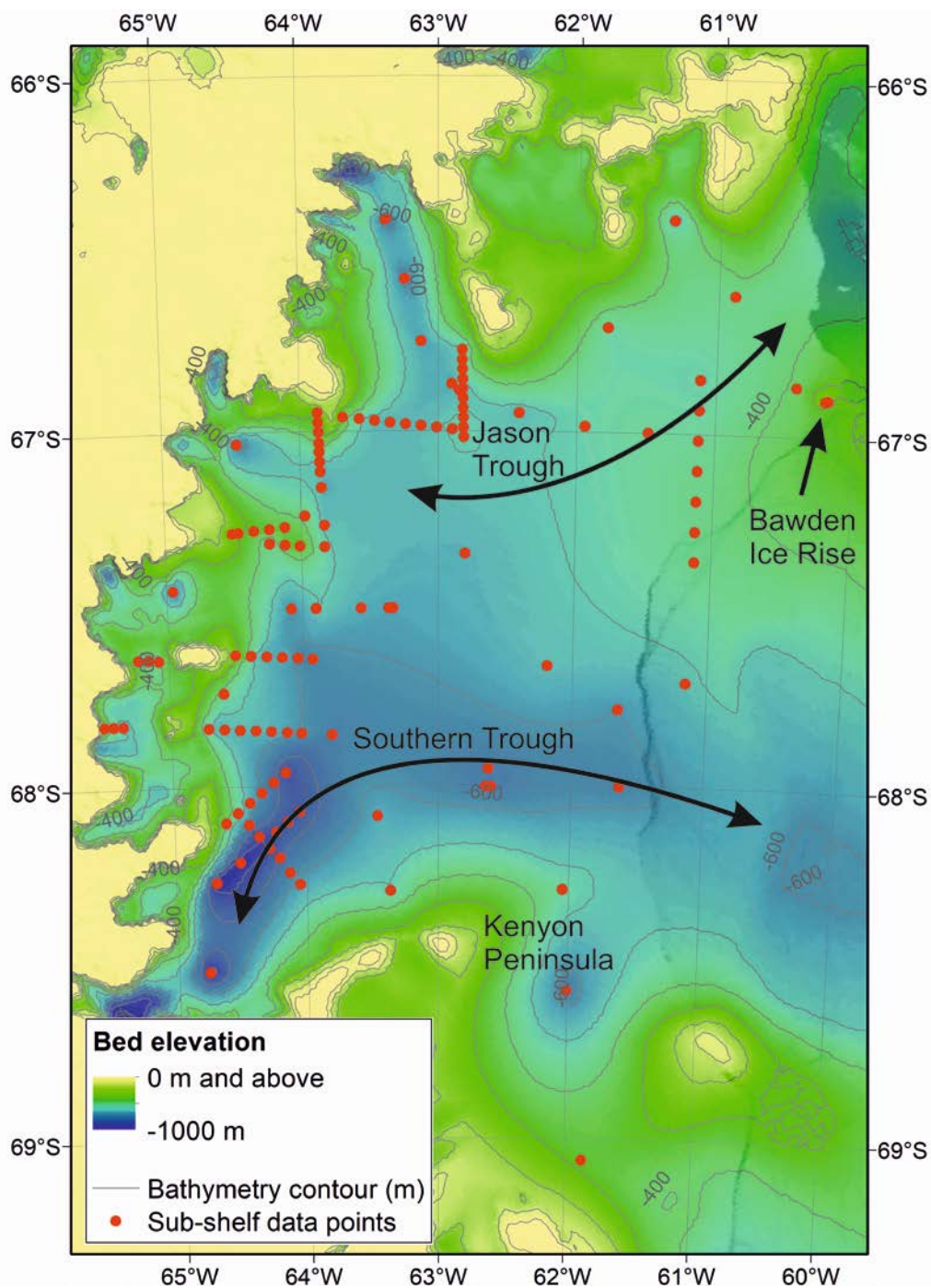
Figure 3 Updated bathymetry map of Larsen C Ice Shelf with large-scale features highlighted. For clarity, elevations above 0 m are unscaled and we label only the -400 and -600 m contours. The background is MODIS imagery from 20th December 2018 highlighting the new ice shelf front following the calving of iceberg A68.

References

Ashmore, D. W., Hubbard, B., Luckman, A., Kulessa, B., Bevan, S., Booth, A., Munneke, P. K., O'Leary, M., Sevestre, H., and Holland, P. R.: Ice and firn heterogeneity within Larsen C Ice Shelf from borehole optical televiewing, 122, 1139-1153, 10.1002/2016jf004047, 2017.

5   Booth, A.: Seismic refraction data, Antarctic Peninsula, Larsen C Ice Shelf, Whirlwind Inlet, November-December 2015 [Data set], UK Polar Data Centre, Natural Environment Research Council, UK Research & Innovation, 10.5285/5D63777D-B375-4791-918F-9A5527093298, 2019.

Booth, A., White, J., Pearce, E., Cornford, S., Brisbourne, A., Luckman, A., and Kulessa, B.: Seismic refraction data from two sites on Antarctica's Larsen C Ice Shelf, Nov 2017, following the calving of Iceberg A68 [Data set], UK Polar Data Centre,
10   Natural Environment Research Council, UK Research & Innovation, 10.5285/147BAF64-B9AF-4A97-8091-26AEC0D3C0BB, 2019.

Brisbourne, A., Hudson, T., and Holland, P.: Seismic bathymetry data, Antarctic Peninsula, Larsen C Ice Shelf, 2016 [Data set], UK Polar Data Centre, Natural Environment Research Council, UK Research & Innovation, 10.5285/315740B1-A7B9-4CF0-9521-86F046E33E9A, 2019.

15   Brisbourne, A. M., Smith, A. M., King, E. C., Nicholls, K. W., Holland, P. R., and Makinson, K.: Seabed topography beneath Larsen C Ice Shelf from seismic soundings, The Cryosphere, 8, 1-13, 10.5194/tc-8-1-2014, 2014.

Cochran, J. R., and Bell, R. E.: Inversion of IceBridge gravity data for continental shelf bathymetry beneath the Larsen Ice Shelf, Antarctica, J. Glaciol., 58, 540-552, 10.3189/2012JoG11J033, 2012.

Cook, A. J., and Vaughan, D. G.: Overview of areal changes of the ice shelves on the Antarctic Peninsula over the past 50
20   years, Cryosphere, 4, 77-98, 10.5194/tc-4-77-2010, 2010.

Forste, C., Schmidt, R., Stubenvoll, R., Flechtner, F., Meyer, U., Konig, R., Neumayer, H., Biancale, R., Lemoine, J. M., Bruinsma, S., Loyer, S., Barthelmes, F., and Esselborn, S.: The GeoForschungsZentrum Potsdam/Groupe de Recherche de Geodesie Spatiale satellite-only and combined gravity field models: EIGEN-GL04S1 and EIGEN-GL04C, Journal of Geodesy, 82, 331-346, 10.1007/s00190-007-0183-8, 2008.

25   Fretwell, P., Pritchard, H. D., Vaughan, D. G., Bamber, J. L., Barrand, N. E., Bell, R., Bianchi, C., Bingham, R. G., Blankenship, D. D., Casassa, G., Catania, G., Callens, D., Conway, H., Cook, A. J., Corr, H. F. J., Damaske, D., Damm, V., Ferraccioli, F., Forsberg, R., Fujita, S., Gim, Y., Gogineni, P., Griggs, J. A., Hindmarsh, R. C. A., Holmlund, P., Holt, J. W., Jacobel, R. W., Jenkins, A., Jokat, W., Jordan, T., King, E. C., Kohler, J., Krabill, W., Riger-Kusk, M., Langley, K. A., Leitchenkov, G., Leuschen, C., Luyendyk, B. P., Matsuoka, K., Mouginot, J., Nitsche, F. O., Nogi, Y., Nost, O. A., Popov, S.
30   V., Rignot, E., Rippin, D. M., Rivera, A., Roberts, J., Ross, N., Siegert, M. J., Smith, A. M., Steinhage, D., Studinger, M., Sun, B., Tinto, B. K., Welch, B. C., Wilson, D., Young, D. A., Xiangbin, C., and Zirizzotti, A.: Bedmap2: improved ice bed, surface and thickness datasets for Antarctica, The Cryosphere, 7, 375-393, 10.5194/tc-7-375-2013, 2013.

Grosfeld, K., Gerdes, R., and Determann, J.: Thermohaline circulation and interaction between ice shelf cavities and the adjacent open ocean, J. Geophys. Res.-Oceans, 102, 15595-15610, 10.1029/97jc00891, 1997.

35   Holland, P. R., Brisbourne, A., Corr, H. F. J., McGrath, D., Purdon, K., Paden, J., Fricker, H. A., Paolo, F. S., and Fleming, A. H.: Oceanic and atmospheric forcing of Larsen C Ice-Shelf thinning, The Cryosphere, 9, 1005-1024, 10.5194/tc-9-1005-2015, 2015.

Howat, I. M., Porter, C., Smith, B. E., Noh, M. J., and Morin, P.: The Reference Elevation Model of Antarctica, The Cryosphere, 13, 665-674, 10.5194/tc-13-665-2019, 2019.

40   Hubbard, B., Luckman, A., Ashmore, D. W., Bevan, S., Kulessa, B., Kuipers Munneke, P., Philippe, M., Jansen, D., Booth, A., Sevestre, H., Tison, J.-L., O'Leary, M., and Rutt, I.: Massive subsurface ice formed by refreezing of ice-shelf melt ponds, Nature Communications, 7, 11897, 10.1038/ncomms11897, 2016.

Jacobs, S. S.: Bottom water production and its links with the thermohaline circulation, Ant. Sci., 16, 427-437, 2004.

Jansen, D., Luckman, A. J., Cook, A., Bevan, S., Kulessa, B., Hubbard, B., and Holland, P. R.: Brief Communication: Newly
45   developing rift in Larsen C Ice Shelf presents significant risk to stability, The Cryosphere, 9, 1223-1227, 10.5194/tc-9-1223-2015, 2015.

Jenkins, A., Dutrieux, P., Jacobs, S. S., McPhail, S. D., Perrett, J. R., Webb, A. T., and White, D.: Observations beneath Pine Island Glacier in West Antarctica and implications for its retreat, Nat. Geosci., 3, 468-472, 10.1038/ngeo890, 2010.

Jullion, L., Garabato, A. C. N., Meredith, M. P., Holland, P. R., Courtois, P., and King, B. A.: Decadal Freshening of the
50   Antarctic Bottom Water Exported from the Weddell Sea, J. Clim., 26, 8111-8125, 10.1175/Jcli-D-12-00765.1, 2013.

Khazendar, A., Borstad, C. P., Scheuchl, B., Rignot, E., and Seroussi, H.: The evolving instability of the remnant Larsen B Ice Shelf and its tributary glaciers, Ear. Planet. Sci. Let., 419, 199-210, 10.1016/j.eps1.2015.03.014, 2015.

Kirchner, J. F., and Bentley, C. R.: RIGGS III: Seismic short-refraction studies using an analytical curve-fitting technique, Ant. Res. Series, 42, 109-126, 1990.

5   Kohnen, H.: The temperature dependence of seismic waves in ice, J. Glaciol., 13, 144-147, 1974.

Kulessa, B.: Seawater softening of suture zones inhibits fracture propagation in Antarctic ice shelves, Nat. Comms, Accepted, 2019.

Kulessa, B., and Bevan, S.: Seismic refraction data, Antarctic Peninsula, Larsen C Ice Shelf, Cabinet Inlet, November-December 2014 [Data set], UK Polar Data Centre, Natural Environment Research Council, UK Research & Innovation,
10   10.5285/FFF8AFEE-4978-495E-9210-120872983A8D, 2019.

Mueller, R. D., Padman, L., Dinniman, M. S., Erofeeva, S. Y., Fricker, H. A., and King, M. A.: Impact of tide-topography interactions on basal melting of Larsen C Ice Shelf, Antarctica, J. Geophys. Res.-Oceans, 117, 10.1029/2011jc007263, 2012.

Nicholls, K. W., Makinson, K., and Venables, E. J.: Ocean circulation beneath Larsen C Ice Shelf, Antarctica from in situ observations, Geophys. Res. Let., 39, 10.1029/2012gl053187, 2012.

15   Nost, O. A.: Measurements of ice thickness and seabed topography under the Fimbul Ice Shelf, Dronning Maud Land, Antarctica, J. Geophys. Res.-Oceans, 109, 10.1029/2004jc002277, 2004.

Rignot, E., Casassa, G., Gogineni, P., Krabill, W., Rivera, A., and Thomas, R.: Accelerated ice discharge from the Antarctic Peninsula following the collapse of Larsen B ice shelf, Geophys. Res. Let., 31, 10.1029/2004gl020697, 2004.

Rosier, S. H. R., Hofstede, C., Brisbourne, A. M., Hattermann, T., Nicholls, K. W., Davis, P. E. D., Anker, P. G. D.,
20   Hillenbrand, C. D., Smith, A. M., and Corr, H. F. J.: A New Bathymetry for the Southeastern Filchner-Ronne Ice Shelf: Implications for Modern Oceanographic Processes and Glacial History, Journal of Geophysical Research: Oceans, 123, 4610-4623, 10.1029/2018JC013982, 2018.

Rott, H., Rack, W., Nagler, T., and Skvarca, P.: Climatically induced retreat and collapse of northern Larsen Ice Shelf, Antarctic Peninsula, Ann. Glaciol., 27, 86-92, 1998.

25   Scambos, T. A., Bohlander, J. A., Shuman, C. A., and Skvarca, P.: Glacier acceleration and thinning after ice shelf collapse in the Larsen B embayment, Antarctica, Geophys. Res. Let., 31, L18402, 10.1029/2004gl020670, 2004.

Scambos, T. A., Haran, T. M., Fahnestock, M. A., Painter, T. H., and Bohlander, J.: MODIS-based Mosaic of Antarctica (MOA) data sets: Continent-wide surface morphology and snow grain size, Remote Sens. Environ., 111, 242-257, 10.1016/j.rse.2006.12.020, 2007.

30   Skvarca, P., Rack, W., Rott, H., and Donangelo, T. I. Y.: Climatic trend and the retreat and disintegration of ice shelves on the Antarctic Peninsula: an overview, Polar Res., 18, 151-157, 1999.

Vaughan, D. G., and Doake, C. S. M.: Recent atmospheric warming and retreat of ice shelves on the Antarctic Peninsula, Nature, 379, 328-331, 10.1038/379328a0, 1996.

Voigt, D. E., Peters, L. E., and Anandakrishnan, S.: 'Georods': the development of a four-element geophone for improved
35   seismic imaging of glaciers and ice sheets, Ann. Glaciol., 54, 142-148, 10.3189/2013AoG64A432, 2013.

Table 1 Field acquisition parameters for new data presented here. Due to the use of a range of acquisition geometries, the specific geometry used at every refraction experiment site is included in the data repository.

Acquisition parameter	BAS Bathymetry	BAS Refraction	MIDAS Refraction	SOLIS Refraction	RACE Reflection
Source type	Hammer	Pentolite (surface)	Hammer	Pentolite (1 m depth)	Hammer
Trigger type	Uphole geophone	Blaster initiated	Impact-sensitive switch	Blaster initiated	Impact-sensitive switch
Receiver type	Georod	Georod	Geophone	Geophone	Geophone
Receiver corner frequency	40 Hz	40 Hz	100 Hz	100 Hz	10 Hz
Receiver spacing	10 m; 30 m offset to first receiver	2.5m to 10m; 5m to 30m; 10m thereafter	48 channels increasing from 0.5 to 10m*	2.5m to 10m; 5m to 30m; 10m thereafter	10 m
Maximum offset (m)	260	610	1110	1110	330
Sample interval (ms)	0.125	0.125	0.0625	0.0625	0.0625
Record length (s)	2	2	1	1	1

Table 2 Location and seabed depth measurements of all new points used in this study.

SITE	Project	Latitude (°)	Longitude (°)	Elevation (m)	Ice shelf thickness (m)	Water column thickness (m)	Seabed elevation (m)
SLGS	SOLIS	-68.005	-62.642	55.00	302.4	410.4	-657.8
SLGN	SOLIS	-67.954	-62.624	53.00	300.8	410.4	-658.1
CI-0-wet	MIDAS	-66.403	-63.376	76.87	559.3	176.5	-659.0
CI-0-dry	MIDAS	-66.402	-63.371	70.62	577.3	173.4	-680.1
CI-20	MIDAS	-66.571	-63.238	66.73	499.3	213.8	-646.4
CI-40	MIDAS	-66.746	-63.121	56.21	439.9	192.2	-575.9
CI-60	MIDAS	-66.885	-62.847	49.74	366.4	222.2	-538.9
CI-80	MIDAS	-66.948	-62.415	48.05	301.2	282.5	-535.6
CI-100	MIDAS	-66.984	-61.939	48.05	277.9	243.2	-473.0
CI-120	MIDAS	-67.000	-61.481	47.21	262.2	237.5	-452.5
WI-70	MIDAS	-67.500	-63.336	49.00	297.6	326.4	-575.0
WI-60	MIDAS	-67.500	-63.569	49.65	283.9	324.0	-558.2
WI-45	MIDAS	-67.500	-63.901	49.70	303.0	242.0	-495.3
WI-00	MIDAS	-67.444	-64.953	59.10	445.8	254.9	-641.6
PRHA01	BAS	-67.346	-62.803	52.44	282.5	317.7	-547.7
PRHA02	BAS	-67.662	-62.189	51.24	267.4	312.0	-528.2
PRHA03	BAS	-66.609	-60.884	46.00	211.3	262.2	-427.5
PRHA04	BAS	-66.705	-61.785	47.19	236.3	280.1	-469.2
PRHA05	BAS	-68.294	-62.048	48.15	236.5	269.7	-458.1
PRHA07	BAS	-66.860	-60.424	43.83	235.1	200.3	-391.5
PRHB01	BAS	-68.525	-64.761	78.08	547.9	382.4	-852.2
PRHB02	BAS	-68.088	-63.458	58.32	329.1	293.2	-564.0
PRHB03	BAS	-68.002	-61.634	48.95	266.8	417.0	-634.9
PRHB04	BAS	-68.582	-62.006	27.55	130.0	551.4	-653.8
PRHB05	BAS	-69.062	-61.864	38.87	146.2	224.0	-331.3
PRHB06	BAS	-67.034	-64.460	48.83	277.4	426.3	-654.9
PRHB12	BAS	-67.705	-61.156	47.72	228.1	338.2	-518.6
PRHB15	BAS	-66.400	-61.328	51.54	277.6	307.7	-533.7
RACE-S1	RACE	-67.783	-61.657	50.35	274.9	375.1	-599.7
RACE-S2	RACE	-68.005	-62.600	53.65	297.9	413.1	-657.3

Appendix A

Table A1 Previously published seabed depth measurements included in the gridding process (Holland et al., 2015; Brisbourne et al., 2014)

Latitude (°)	Longitude (°)	Depth (m)	Latitude (°)	Longitude (°)	Depth (m)	Latitude (°)	Longitude (°)	Depth (m)
-67.500	-64.083	-615.9	-67.286	-64.508	-327.0	-68.102	-64.140	-758.8
-67.500	-63.366	-577.6	-66.947	-63.872	-334.3	-68.074	-64.049	-748.7
-67.017	-62.813	-479.2	-66.975	-63.869	-341.8	-68.104	-64.607	-428.7
-66.990	-62.816	-483.6	-67.002	-63.867	-341.2	-68.076	-64.515	-449.3
-66.962	-62.817	-481.3	-67.033	-63.863	-414.0	-68.048	-64.424	-572.7
-66.935	-62.818	-506.9	-67.058	-63.861	-420.8	-68.019	-64.332	-614.7
-66.907	-62.820	-523.4	-67.086	-63.858	-501.7	-67.991	-64.242	-703.6
-66.880	-62.821	-529.1	-67.114	-63.855	-530.6	-67.962	-64.151	-768.8
-66.853	-62.823	-493.5	-67.158	-63.849	-555.0	-68.109	-64.435	-639.6
-66.826	-62.824	-474.8	-67.265	-63.829	-528.3	-68.143	-64.360	-799.6
-66.798	-62.825	-494.2	-67.326	-63.830	-481.6	-68.177	-64.283	-794.3
-66.771	-62.827	-513.1	-67.642	-63.930	-620.6	-68.204	-64.206	-702.5
-66.960	-63.689	-382.6	-67.639	-64.041	-650.6	-68.246	-64.129	-621.2
-66.965	-63.570	-500.7	-67.637	-64.156	-534.9	-68.280	-64.053	-577.5
-66.971	-63.459	-546.1	-67.634	-64.273	-585.1	-66.894	-60.193	-124.8
-66.976	-63.346	-541.6	-67.631	-64.389	-477.5	-66.894	-60.194	-122.2
-66.980	-63.234	-522.7	-67.629	-64.505	-236.0	-66.894	-60.195	-129.7
-66.985	-63.122	-557.5	-67.857	-63.794	-641.0	-66.894	-60.196	-123.6
-66.990	-63.009	-498.8	-67.852	-64.023	-599.8	-66.894	-60.197	-124.7
-66.994	-62.897	-492.9	-67.849	-64.131	-586.2	-66.894	-60.198	-123.9
-66.847	-61.114	-479.7	-67.846	-64.249	-539.9	-66.895	-60.199	-119.2
-66.932	-61.116	-466.2	-67.843	-64.366	-540.1	-66.895	-60.200	-126.6
-67.018	-61.117	-454.0	-67.841	-64.484	-531.8	-66.895	-60.201	-126.7
-67.104	-61.119	-434.0	-67.838	-64.601	-547.7	-66.895	-60.202	-125.1
-67.190	-61.120	-434.0	-67.835	-64.718	-532.0	-66.895	-60.203	-123.9
-67.276	-61.121	-424.6	-67.737	-64.599	-448.5	-66.895	-60.204	-123.2
-67.362	-61.123	-432.7	-67.636	-65.229	-496.6	-66.895	-60.204	-122.5
-67.323	-64.012	-316.0	-67.638	-65.153	-481.5	-66.895	-60.205	-120.3
-67.320	-64.120	-321.3	-67.640	-65.075	-490.6	-66.895	-60.206	-128.1
-67.316	-64.235	-461.1	-67.823	-65.502	-392.3	-66.895	-60.207	-126.6
-67.238	-63.973	-413.1	-67.823	-65.431	-567.8	-66.895	-60.208	-127.2
-67.270	-64.120	-358.9	-67.823	-65.361	-625.6	-66.896	-60.209	-127.7
-67.275	-64.234	-328.2	-68.272	-64.692	-868.1	-66.896	-60.210	-130.7
-67.279	-64.348	-314.3	-68.216	-64.507	-856.2	-66.896	-60.211	-133.6
-67.284	-64.462	-306.3	-68.130	-64.231	-763.4	-66.896	-60.212	-136.7
						-66.896	-60.213	-137.5